CATALYTIC REMOVAL OF CHLORINATED COMPOUNDS OVER ORDERED MESOPOROUSCOBALT OXIDES SYNTHESISED BY HARD-TEMPLATING

J. González Prior, R. López-Fonseca, J.I. Gutiérrez-Ortiz, B. de Rivas

Applied Catalysis B: Environmental 222 (2018) 9–17

DOI: 10.1016/j.apcatb.2017.09.050

CATALYTIC REMOVAL OF CHLORINATED COMPOUNDS OVER ORDERED MESOPOROUS COBALT OXIDES SYNTHESISED BY HARD-TEMPLATING

J. González-Prior, R. López-Fonseca, J.I. Gutiérrez-Ortiz, B. de Rivas*

Chemical Technologies for Environmental Sustainability Group,
Department of Chemical Engineering, Faculty of Science and Technology,
University of The Basque Country (UPV/EHU), PO Box 644, E-48080 Bilbao, Spain.

*Corresponding author:
Phone: +34-94-6015553
Fax: +34-94-6015963
E-mail address: beatriz.derivas@ehu.eus

18 **GRAPHICAL ABSTRACT**

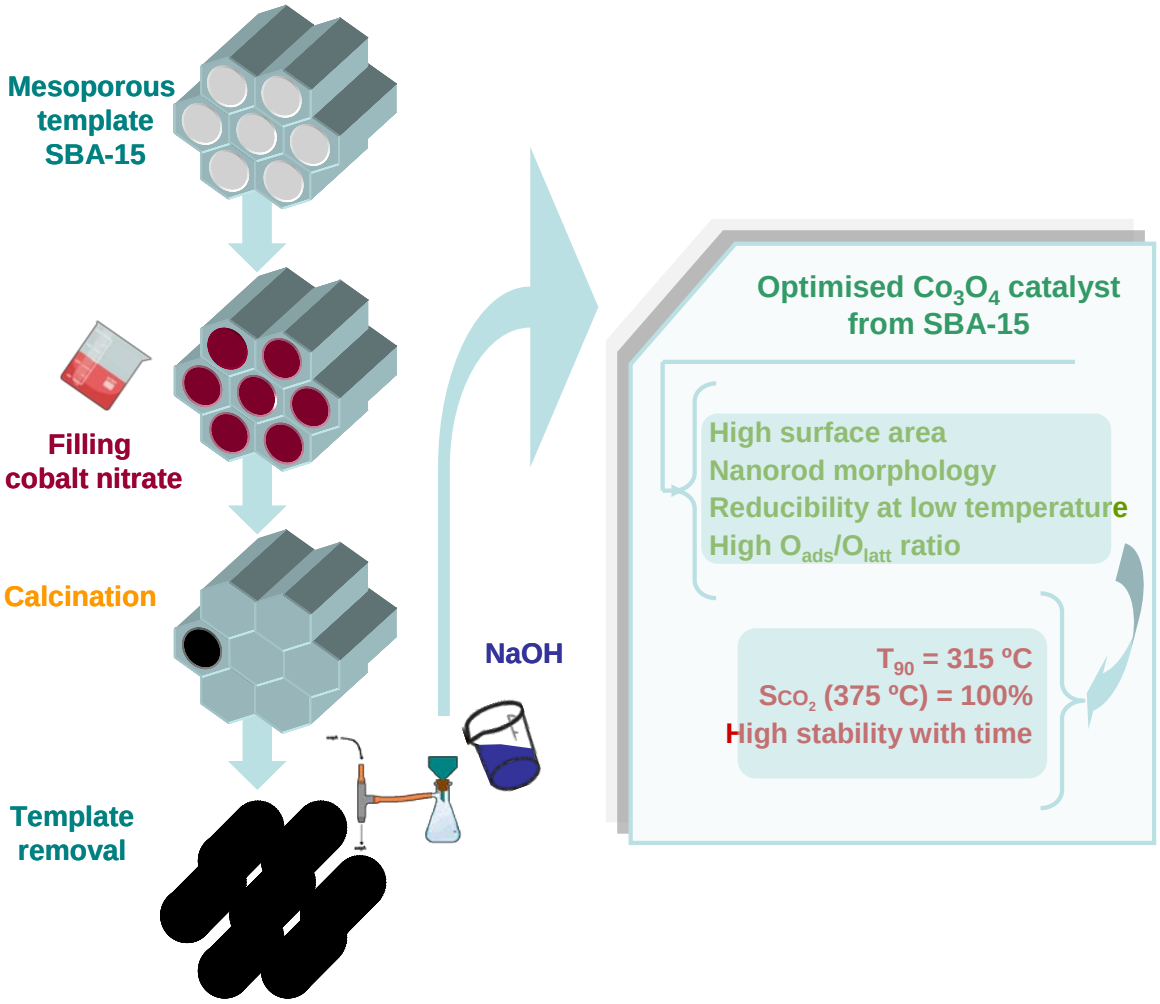

ABSTRACT

This work evaluates the catalytic behaviour of a series of mesoporous bulk cobalt oxide prepared by hard-templating using SBA-15, SBA-16 and SBA-3. In addition, a bulk catalyst obtained by silica aquagel confined precipitation is also examined. The oxidation of 1,2-dichloroethane has been selected as a model reaction for determining their suitability for the efficient removal of chlorinated pollutants in gaseous waste streams.

The catalytic behaviour is found to depend on the abundance of surface adsorbed oxygen species and a good low-temperature reducibility. These key physico-chemical properties are optimised for nanocasted Co_3O_4 prepared by using SBA-15 as hard template. This sample is characterised by a relatively high surface area, a nanorod-like morphology and a high quality 2D ordered mesoporous structure. At 375-400 ºC this sample attains an efficient oxidation of the chlorinated feed to CO_2 and HCl/Cl_2 while keeping a reasonable stability with time.

Keywords: catalytic oxidation, 1,2-dichloroethane, hard-templated cobalt oxide, oxygen mobility, 2D ordered nanorods

1. Introduction

Chlorinated organic compounds, which are emitted from a wide range of industrial processes, such as polymer synthesis and processing, production of pesticides, solvents, insulators or electronic devices, are linked with the formation of low-level ozone and photochemical smog, stratospheric ozone depletion, and are considered greenhouse gases. Catalytic combustion is accepted as an attractive technology for removal at low temperatures when operating with dilute effluent streams. The proper catalyst selection and subsequent optimisation are essential for achieving efficient oxidation.

In order to avoid the use of noble metals in the catalyst formulation, substantial efforts have made in the design of suitable alternatives in terms of activity and cost. In this sense, much interest has been given to the development of Co_3O_4-based catalysts due to their notable performance in comparison with other transition metal oxides [1,2]. The catalytic activity of Co_3O_4 is essentially related to its surface area, pore structure, oxygen nonstoichiometry, and reducibility [3]. These properties in turn are intimately related to the surface morphology and the exposed crystal planes of the spinel. All these physico-chemical features can be optimised by the preparation method [4,5].

As an alternative to conventional and soft-templating synthesis routes, the hard-templating method is an attractive route for the synthesis of mesoporous Co_3O_4. Ordered mesopores silica is especially adequate as solid template for obtaining structured materials owing to its highly tailorable textural properties [6]. In addition to leading to bulk catalysts with a relatively high surface area and a controllable pore structure, which are derived from replication of the pore system of the template, the nanomorphology can be tuned. Besides the channels of the template may induce a positive confinement effect on the predominantly exposed planes [7,8].

The objective of this work is the synthesis, characterisation and evaluation of a series of mesopores bulk cobalt oxide catalysts for the oxidation of 1,2-dichloroethane ($C_2H_4Cl_2$, DCE), which has been chosen as a model chlorinated pollutant. More particularly, the effect of the selection of the silica template (SBA-15, SBA16 and SBA-3) on the physico-chemical properties of the nanocasted Co_3O_4 has been analysed.

2. Experimental

2.1. Template preparation

Three different silicas, namely SBA-15, SBA-3 and SBA-16, were synthesised and subsequently used as hard-templates for the preparation of Co_3O_4 catalysts. The SBA-15 and SBA-3 are mesoporous silicas templates with a two-dimensional p6mm cubic arrangement of pores. SBA-15 shows hexagonal pores in a 2D array with long 1D channels (p6mm plane group). The channels are interconnected by small micropores. SBA-3 has a uniformly ordered pore structure with a linear channel array of mesopores, with a 2D hexagonal structure. The SBA-16 matrix is a material with a 3D cubic arrangement of mesopores corresponding to the Im3m space group. Each mesopore in this body-centered cubic structure is connected with its eight nearest neighbors. These materials were prepared according to the synthesis procedures described in the literature, namely SBA-15 [9,10] and SBA-3 and SBA-16 [5,11].

2.2. Synthesis of hard-templated samples

Using these three silicas as templates (SBA-15, SBA-3 and SBA-16), different Co_3O_4 catalysts were prepared by means of wet impregnation method under reduced pressure using a rotary evaporator. An aqueous solution (100 cm^3) of cobalt (II) nitrate was used, with a Co/Si molar ratio of 0.25. In an attempt to examine the effect of this parameter, the SBA-15 silica was also impregnated with a more concentrated aqueous solution, with a Co/Si molar ratio of 0.4. In this case, the pores of the silica were expected to be

completely filled and some cobalt oxide were likely formed out of the silica structure. This was confirmed by the notable decrease in surface area observed for this sample (320 $m^2 g^{-1}$) in comparison with that of the impregnated sample with a lower Co/Si molar ratio (440 $m^2 g^{-1}$). On the other hand, an additional cobalt oxide catalyst was prepared by silica aquagel confined coprecipitation (the so-called SACOP method). Thus, the precursor of the metal oxide was introduced in the cast during the synthesis step of the silica. The catalyst was obtained by mixing sodium silicate, hydrochloric acid, distilled water and cobalt nitrate hexahydrate with a $SiO_2/Co/H^+/H_2O$ molar ratio of 1/0.25/6.54/193.9 for 24 h. Then, the mixture was transferred to an autoclave under hydrothermal conditions at 100 ºC for additional 24 h. Next, the metal hydroxide was precipitated with NaOH 3.5 mol L^{-1}. Finally, the solid was washed, dried and calcined at 500 ºC [12].

Finally, once the cobalt oxide was inside the pores of the various silicas, the matrix was removed using NaOH 2 mol L^{-1}. This step was repeated four times allowing for obtaining nanocasted pure cobalt oxide. All samples were then washed several times with distilled water to remove the remaining NaOH and then dried at 110 °C overnight. Thus, the Co-S15 sample was obtained from the cobalt oxide impregnated on the SBA-15 silica. When using a higher Co/Si molar ratio (0.4) the sample was labelled as Co-S15(0.4). Similarly, the Co-S3 and Co-S16 oxides were prepared using SBA-3 and SBA-16 silicas, respectively while the Co-SP oxide was the sample synthesised by the SACOP method.

2.3. Characterisation techniques

Textural properties were evaluated from the nitrogen adsorption-desorption isotherms, determined at -196 °C with a Micromeritics TRISTAR II apparatus. The specific surface areas of the samples were determined in line with standard BET procedure. The

mean pore size was calculated using the BJH method. The samples were previously degassed overnight with N_2 flow.

X-ray diffraction (XRD) studies were carried out on a X'PERT-MPD X-ray diffractometer with Cu Kα radiation (λ = 1.5406 Å) and Ni filter. The X-ray tube was operated at 30 kV and 20 mA. Samples were scanned from $5° < 2\theta < 80°$ and the X-ray diffraction line positions were determined with a step size of 0.02° and counting time of 2.5 s per step. Phase identification was conducted by comparison with ICDD (International Centre for Diffraction Data) database cards.

Transmission electron microscopy (TEM) investigations were performed using a Philips CM200 microscope equipped with LaB6 crystal as electron source and operating at 200 kV. Bright field images were acquired using a high resolution CCD camera. Drops of emulsions, created by sonication of the powder samples in ethanol, were deposited on C coated Cu grids and left in air to dry. HRTEM measurements were carried out with a FEI Titan Cubed G2 60-300 electron microscope at 300 kV equipped with a high-brightness X-FEG Schottky field emission electron gun and a monochromator and CEOS GmbH spherical aberration (Cs) corrector on the image side. The images were recorded on a charge-coupled device (CCD) camera (2kx2k Gatan UltraScanTM 1000). The sample was prepared by dispersion into ethanol solvent and keeping the suspension in an ultrasonic bath for 15 min, after a drop of suspension was spread onto a TEM copper grid (300 mesh) covered by a holey carbon film followed by drying under vacuum.

X-ray photoelectron spectroscopy studies were performed using in a SPECS system with equipped with Phoibos 150 1D analyzer and DLD-monochromatic radiation source.

The IR spectra were recorded on a Thermo Scientific Nicolet 380 FT-IR spectrometer in the range of 4000-400 cm^{-1}. The skeletal characterization was carried out diluting 1 mg of each powder with 100 mg of IR-grade KBr powder finely mixed in an agate mortar and subjected to a pressure of 2 ton to obtain suitable self-supporting disks for the IR analysis.

Redox behaviour was examined by temperature-programmed reduction experiments (TPR) with hydrogen. These experiments were conducted on a Micromeritics Autochem 2920 instrument. Firstly, all the samples (20 mg) were pre-treated in an oxygen stream (5%O_2/He) at 400 °C for 1 h, and then cooled down to room temperature. The reducing gas used in all experiments was 5%H_2 in Ar, with a flow rate of 50 cm^3 min^{-1}. The temperature range explored was from room temperature to 600 °C with a heating rate of 10 °C min^{-1}. This temperature was held for 0.5 h. The water produced by the reduction process was trapped into a cold trap. The consumption of H_2 was quantitatively measured by time integration of TPR profiles. The calibration sample for quantitative analysis of H_2 uptake was silver oxide.

The total acidity of the catalysts was evaluated by NH_3 adsorption at 100 °C followed by thermogravimetry. These experiments were carried out with a Setaram Setsys Evolution thermobalance under atmospheric pressure coupled to a Pfeiffer Prisma mass spectrometer. Prior to adsorption experiments, the samples were first pretreated in a helium stream at 500 °C (10 °C min^{-1}) and then cooled to 100 °C (40 °C min^{-1}). Later, the NH_3 adsorption step was performed by admitting a flow of 10% NH_3/He at 100 °C up to saturation. Subsequently, the samples were exposed to a flow of helium (50 cm^3 min^{-1}) for 2 h at 100 °C to remove reversibly and physically bound ammonia from the surface. The mass variation and the sample temperature were continuously recorded by a computerised data acquisition system. The net weight gain was

161 considered as the total acidity of the samples. Then, the temperature was increased from
162 100 to 500 ºC at a constant heating rate of 10 ºC min^{-1}. The exit stream was analysed by
163 on-line mass spectrometry.

164 2.4. Catalyst activity determination

165 Catalytic tests were performed in a bench-scale fixed bed reactor (Microactivity
166 modular laboratory system provided by PID Eng&Tech S.L.) operated at atmospheric
167 pressure and fully monitored by computer. The reactor is made of quartz with an
168 internal diameter of 10 mm and a height of 300 mm, in which the temperature is
169 measured with a thermocouple placed in the catalyst bed. Typically, 0.85 g of catalyst in
170 powdered form (0.3–0.5 mm) was loaded. No quartz sands mixed with the catalyst were
171 used. The reaction feed consisted of 1000 ppm of DCE in dry air with a total gas flow of
172 500 cm^3 min^{-1}. The corresponding gas hourly space velocity was 30,000 h^{-1}. The
173 amount and particle size of catalyst and the total gas flow rate were chosen in order to
174 be out of the internal and external diffusion limits. Catalytic activity was measured over
175 the range 150-500 °C and conversion data were calculated by the difference between
176 inlet and outlet concentrations. Conversion measurements and product profiles were
177 taken at steady state, typically after 30 min on stream. Either product selectivity was
178 calculated based on either chlorine or carbon atoms present in that product divided by
179 the total chlorine or carbon atoms present in the product stream (expressed as %). The
180 feed and effluent stream were analysed using an on-line 7980A Agilent Technologies
181 gas chromatograph equipped with a thermal conductivity detector (CO and CO_2) and an
182 electron capture detector (chlorinated hydrocarbons). Analysis of HCl and Cl_2 was
183 carried out by means of ion selective electrode and titration, respectively. Further details
184 on analytical procedures are described elsewhere [13].
185

3. Results

3.1. Characterisation of the hard-templated Co_3O_4 catalysts

The textural properties of the synthesised silicas used as hard templates were previously examined. Their BET surface area, pore volume and average pore size are summarised in Table 1. The corresponding N_2 physisorption isotherms and pore size distribution are included in Figures S1 and S2 (supplementary material). The SBA-3 silica exhibited a noticeable lower surface about 260 m^2 g^{-1} in comparison with that exhibited by both SBA-15 and SBA-16 materials, with a surface area of 750 and 785 m^2 g^{-1}, respectively. The three samples presented a type IV isotherm. In this sense, an ordered mesoporous structure of these siliceous materials was directly evidenced by TEM (Figure 1). The N_2 isotherm of SBA-16, with a broad H2-type hysteresis loop and a unimodal pore size distribution at 39 Å, was comparable to that reported in the literature [14]. However, the expected well-defined H1-type hysteresis loop with almost vertical and parallel adsorption-desorption branches was not obtained for the as-synthesised SBA-15, probably due its non-uniform pore size pore size distribution [15]. Note that, in addition to a main peak centred at 39 Å, a shoulder at around 56 Å was also observed. On the other hand, a much larger pore size of 125 Å (typically 30 Å for this kind of materials), and consequently a markedly low surface area were found for SBA-3 [16]. This was probably due to the high CTAB:TEOS molar ratio (3.6) used in the synthesis.

FIGURE 1

TABLE 1

A set of hard templated cobalt oxide catalysts were obtained after impregnation followed by calcination and subsequent silica removal with sodium hydroxide. Results included in Table 1 pointed out that small amounts of SiO_2 between 1.2 and 3.6wt% were still presented in the Co-S3, Co-S15(0.4), Co-S15 and Co-S16 catalysts. The

presence of residual silica was in agreement with the results given by other authors who pointed out that the remaining silica was very likely trapped among the crystallites of Co_3O_4 [17,18]. However, a relatively high amount of SiO_2 close to 7 wt% was found in the case of the Co-SP sample. Hence, the dissolution of silica with NaOH was considerably less efficient for such sample. In agreement with the previous results, TEM analysis coupled to EDX clearly identified the presence of silica particles (Figure S3, supplementary material). On the other hand, no analysis of the used NaOH aqueous solution was carried to check the eventual dissolution of cobalt species.

The structural properties are characterised by XRD using the ICDD files as a reference. Figure 2 shows the XRD patterns of the five samples calcined at 500 ºC. For every catalyst all the reflection peaks, located at 2θ 19º, 31.3º, 36.8º, 44.8º, 59.3º and 65.2º, could be assigned to a pure cubic phase of cobalt (II,III) oxide spinel (PDF 42-1467), irrespectively of the used hard template. No diffraction peaks related to a CoO phase are detected. The average Co_3O_4 crystallite diameters, estimated from the full width at half maximum of the characteristic diffraction peaks by applying the Scherrer equation (Table 1), ranged between 12 and 16 nm for the Co-S15, Co-S16 and Co-SP samples, while a larger crystallite size was found for the Co-S3 and Co-S15(0.4) samples (26 and 29 nm, respectively).

FIGURE 2

Figure 3 includes the TEM images of the as-prepared Co_3O_4 samples after the silica removal. 2D highly ordered mesoporous architectures were found in the two SBA-15-derived bulk catalysts (Figures 3a and 3e). This was probably connected to the fullfilling of the mesopores of the silica matrix with the aqueous solution of cobalt nitrate irrespective of the used Co/Si ratio. As a result, rod-like structures were assumed to be formed inside the silica pores, thereby promoting the crystallite growth with the

same shape as the pores. Interestingly, after the silica removal these morphologies still remained, being reasonable replicas of this silica template. By contrast, a 3D wormhole-like mesoporous structure was noticed for the Co-S3 and Co-S16 catalysts (Figures 3b and 3c, respectively) presumably due to an incomplete coverage of the mesopores or the loss of the structure when the cobalt precursor was incorporated [19,20]. Finally, it must be pointed out that the morphology of the Co-SP sample (Figure 3d) was a mixture of both ordered and wormhole-like structures. These results contrast with those found by Lopez et al. [10] who observed a needle-shaped nanostructure for this type of material. This different morphology could be related to the lower calcination temperature (400 ºC) in comparison with 500 ºC used in this work.

FIGURE 3

The textural properties in terms of BET surface area, pore volume and average pore size of the Co_3O_4 catalysts are shown in Table 1. The corresponding N_2 physisorption isotherms of the hard-templated samples are depicted in Figure S4 (supplementary material). Except for the Co-S3 sample the surface areas of the ordered rods were noticeably lower (62-83 $m^2\ g^{-1}$) than the wormhole-like structures (111-123 $m^2\ g^{-1}$) [19]. It must be pointed out that the contribution of residual silica to the surface area of the samples, while assuming that its original textural properties were preserved after the treatment with NaOH solution, is about 20% (5% for the Co-S3 catalyst). The pore size distribution shown in Figure S5 (supplementary material) also revealed noticeable differences among the synthesised mesoporous materials. Thus, when the SBA-15 silica was used, irrespective of the Co/Si ratio, a unimodal pore distribution was noted with a peak centred at around 35 Å. The mesopores of these samples were formed via the 2D connections of Co_3O_4 skeletons. In the case of Co-S16 a wide pore distribution was found as well but with a slightly larger average size. Thus, the maximum values were

261 located at 53 and 62 Å. On the other hand, when using the SACOP method and the
262 SBA-3 template, the resulting oxides displayed a clear bimodal pore distribution. The
263 Co-SP sample presented pores of a similar size to the other samples, centred at 35 and
264 62 Å, whereas the Co-S3 sample exhibited comparatively much larger pore sizes with
265 peaks located at 160 and 232 Å. The wider pore distribution and consequently the larger
266 average pore size suggested that the mesopores of the Co-S16, Co-S3 and Co-SP oxides
267 were originated from the irregular compiling of Co_3O_4 nanoparticles.
268 XPS analysis was employed to gain further insight into the surface composition, metal
269 oxidation state, and adsorbed species of the prepared bulk oxides. Figure 4 illustrates
270 the Co $2p_{3/2}$ and O 1s XPS spectra of the Co-S15 catalyst as an example. Hence, an
271 asymmetrical Co $2p_{3/2}$ peak, which could be decomposed into three components at a
272 binding energy 779.2, 781.7 and 782.5 eV, was noticed. The first signal was assigned to
273 the surface Co^{3+} species and the second one to surface Co^{2+} species, whereas the latter
274 corresponded to the presence of CoO species on the surface [21]. The contribution of
275 these species were estimated to be roughly similar on the five samples and around than
276 10-15% of the total amount of cobalt. The low intensity peaks that appeared at 785.4
277 and 790.0 eV were characteristic shake-up satellites of CoO and Co_3O_4, respectively
278 [16]. On the other hand, by adopting the curve-fitting method, the asymmetrical O 1s
279 XPS band of each sample could be decomposed into two components. The first signal
280 located at 529.8 eV was attributable to the surface lattice oxygen (O_{latt}) species. The
281 other peak (531 eV) was assigned to adsorbed oxygen (O_{ads} species as O^-, O^{2-} or O_2^{2-})
282 species [20,22]. Table 2 lists the quantitative analysis of the XPS spectra in terms of
283 O_{ads}/O_{latt} and Co^{2+}/Co^{3+} ratios. These were calculated from the relative intensities of the
284 corresponding peaks. A good relationship between surface Co^{2+} and oxygen species
285 concentration was found, in agreement with [20]. The abundance of these species

appreciably decreased according to the following order: Co-S15 > Co-S15(0.4) > Co-S16 > Co-S3 > Co-SP. This notable variation in surface Co^{2+}/Co^{3+} molar ratio, from 1.2 to 0.8, and surface O_{ads}/O_{latt} molar ratio, from 0.98 to 0.64, clearly evidenced that the synthesis method played an important role in determining the surface composition.

FIGURE 4

TABLE 2

The redox properties of cobalt catalysts were investigated by temperature-programmed reduction with hydrogen. The profiles shown in Figure 5 varied appreciably from one sample to another, thus evidencing the existence of various reducible species [17,23]. In all cases the profile could be divided into two zones more or less discernible: one below 300 ºC attributable to the reduction of Co_3O_4 to CoO and another one above this temperature related to the reduction of CoO to Co. This assignation was reasonable since the reduction of Co_3O_4 takes place according to the sequence of $Co_3O_4 \rightarrow CoO \rightarrow Co^0$, with an ideal H_2 uptake of 1:3. In view of the location of the reduction band at low temperatures, the oxygen mobility within the lattice could be indirectly ranked as follows: Co-S15 (250 ºC) > Co-S16 (265 ºC) > Co-S3 (275 ºC) > Co-SP (285 ºC). It should be pointed out that the low-temperatures reducibility occurred in a slightly wider temperature range (250-280 ºC) over the Co-S15(0.4) sample. Therefore, the existence of a higher amount of oxygen defects (evidenced by a high surface Co^{2+}/Co^{3+} ratio) enhanced the oxygen mobility in the lattice as revealed by the promoted reduction at low temperature.

The reduction process of the samples occurred in the 200-525 ºC window, but higher temperatures (600 ºC) were required in the case of the Co-SP sample, thereby pointing out the formation of more stable CoO_x species. The degree of reduction of the samples was calculated based on the fact that 100% of cobalt is present as Co_3O_4. A quantitative

evaluation of the amounts of hydrogen consumed during reduction (about 16.6 mmol H_2 g_{Co3O4}^{-1}) revealed that in all cases Co_3O_4 was converted into metallic cobalt completely, except for the Co-SP catalyst, which only reached a degree of reducibility of about 90%. This suggested the presence of cobalt species (presumably cobalt silicate) which were not reduced below 600 ºC. In this sense, FT-IR studies were carried out to better analyse the skeletal structure of each sample (Figure 6). Thus, the features due to the cobalt-oxygen vibrational modes of cobalt species could be clearly seen. These bands at around 565 and 661 cm^{-1} (with shoulders at higher frequencies) are typical of the Co_3O_4 spinel phase [9,24,25]. They correspond to vibrations of tetrahedral Co^{3+} and octahedral Co^{2+}, respectively, in the spinel structure. In addition, particularly in the Co-SP sample small bands in the 1200-800 cm^{-1} could be detected. The bands in this region are characteristic of silica-based materials. The broad peak centred at 1015 cm^{-1} was associated with the silica support not efficiently removed by NaOH. Moreover, the presence of a peak at around 890 cm^{-1} was assigned to vibrations mode in a cobalt silicate phase [26].

FIGURE 5

FIGURE 6

The overall acidity of the catalysts was evaluated from the net weight gain recorded after an isothermal adsorption step at 100 ºC followed by removal of physisorbed ammonia with an inert stream (Table 1). It was found that the Co-S15 and Co-S16 oxides exhibited a higher total acidity, namely 0.46 and 0.54 mmol NH_3 g^{-1}, respectively, while the remaining three oxides were considerably less acidic, with an overall acidity close to 0.30 mmol NH_3 g^{-1}. The differences among the samples were less apparent when the acid density was compared, since this property varied between 4-6 mmol NH_3 m^{-2}, except for the Co-SP sample, which exhibited a significantly lower

336 value (2.6 mmol NH_3 m^{-2}). The surface reactivity of the catalyst was examined by
337 following the decomposition of this adsorbed probe molecule with increasing
338 temperature under inert conditions. This analysis was carried out by a combined study
339 of the evolution of the weight loss and the composition of the exit stream by mass
340 spectrometry. This investigation could be helpful in evidencing the participation of the
341 oxygen species present in the samples. As an example, the results corresponding to the
342 Co-S16 and Co-SP catalysts are included in Figure 7. These (m/z) MS signals were
343 recorded, namely 15 (NH_3), 18 (H_2O), 28 (N_2), 30 (NO, N_2O or NO_2), 44 (N_2O) and 46
344 (NO_2). At relatively low temperatures the formation of N_2 (m/z=28) was noticed as the
345 main oxidation product ($4NH_3 + 3O_2 \rightarrow 2N_2 + 6H_2O$) [27]. Simultaneously, N_2O
346 (m/z=44) was detected ($2NH_3 + 2O_2 \rightarrow N_2O + 3H_2O$). Since the profile of this signal
347 was identical in shape to that observed for the (m/z=30) signal, the latter was also
348 associated with the presence of N_2O. Accordingly, the presence of NO as oxidation
349 product ($4NH_3 + 5O_2 \rightarrow 4NO + 6H_2O$), which could be also followed by the (m/z=30)
350 signal, was ruled out. The presence of NO_2 ($2NH_3 + 7O_2 \rightarrow 2NO_2 + 3H_2O$) was also
351 negligible as the (m/z=46) signal was flat. Above 300 ºC only trace amounts of
352 ammonia (m/z=15) were detected, probably due to the fact that the active oxygen
353 species were already consumed. Therefore, the unreacted ammonia was desorbed at
354 higher temperatures. It must be stated that no marked differences were noticed in the
355 behaviour of the Co-S15, Co-S16, Co-S3 and Co-S15(0.4) catalysts, since a similar
356 evolution of the product distribution with temperature was noticed. Therefore, the
357 oxidation of adsorbed ammonia was not suitable for identifying the most active catalyst
358 for DCE, presumably owing to the high reactivity of NH_3. Only the Co-SP catalyst
359 exhibited a somewhat lower activity as oxidation products were found at slightly higher
360 temperatures on the basis of the wider temperature window in which N_2 and N_2O were

361 detected. In addition, a favoured formation of N_2O instead of N_2, which occurred at
362 around 300 ºC, was noticed. This was related to its lower population of active oxidation
363 sites at low temperatures. In the case of the other samples, N_2 was detected as the main
364 oxidation product, with a comparable N_2/N_2O formation.

365 FIGURE 7

366 3.2 Behaviour of the hard-templated Co_3O_4 catalysts

367 The catalytic behaviour of the prepared samples was examined by analysing the
368 evolution of the conversion of DCE to CO_2 with the temperatures, which are shown in
369 Figure 8. The corresponding values of T_{50} and T_{90} are summarised in Table 3. The
370 investigated bulk catalysts exhibited a reasonably good performance since in all cases
371 the chlorinated feed was completely abated (100% conversion to CO_2) between 350 and
372 425 ºC, thereby revealing that synthesis routes based on the use of silica as hard
373 template were efficient. Indeed, when compared with our recent results on Co_3O_4
374 prepared via soft-templates [13], these required noticeably higher oxidation
375 temperatures in the 450-500 ºC range. On the other hand, note that the conversion
376 attained over the pure silicas was lower than 5% at 500 ºC.

377 FIGURE 8

378 TABLE 3

379 Judging from the results included in Figure 8 and Table 3, substantial differences in
380 performance were clearly evident as a function of the selected hard template. The
381 temperature required for 50% conversion varied between 270 and 295 ºC, while 90%
382 conversion was attained in the 315-345 ºC range. It was found that the catalysts derived
383 from the SBA-15 exhibited the best behaviour. By contrast, the sample prepared
384 according to the SACOP method showed the poorest performance. Hence, the catalytic
385 conversion, by considering the temperature for 50% conversion, followed this order:

Co-S15 > Co-S15(0.4) > Co-S16 > Co-S3 > Co-SP. These results evidenced that the morphology of the catalysts played an important role for chlorinated VOC oxidation, being the 2D ordered nanorods more efficient than the wormhole-like samples. The observed high activity of nanocasted Co_3O_4 from SBA-15 was agreement with previous reports on the combustion of CO [28] and non-chlorinated VOCs such as benzene [29] and formaldehyde [30]. On the other hand, as for the more recent studied on the decomposition of DCE, Yang et. [31,32] have profusely examined the behavior of various Ce/Cr-based catalysts. When operating at a four times lower space velocity, a T_{50} value (with a selectivity to CO_2 higher than 90%) in the range 210-240 ºC was attained, which was somewhat lower than that attained in this work.

Since the surface areas of the catalysts were considerably different, a more proper comparison of the intrinsic activity of the samples was made in terms of the areal reaction rate ($mmol_{DCE}\ m^{-2}\ h^{-1}$). This specific activity was calculated at 250 ºC, where conversion of the feed to CO_2 was below 20% for all the samples (Table 3). The estimated values were between 0.26 and 0.12 $mmol_{DCE}\ m^{-2}\ h^{-1}$. Note that the activity trend was the same as that noticed as a function of the conversion vs temperature curves. Figure 9 evidences that a good correlation existed between the specific activity and the proportion of Co^{2+} on the surface. As previously demonstrated, a high concentration in the surface of cobalt in low oxidation state (Co^{2+}) could be an indication of oxygen defects close to the surface. Hence, the presence of oxygen deficiencies, which was directly connected with a larger abundance of Co^{2+} ion on the surface, promoted the activation of gas-phase oxygen molecules for the generation of active oxygen species. This relatively large amount of oxygen vacancies in Co_3O_4 nanorods is usually associated with the existence of {220} crystal planes as catalytically active exposed planes [33,34]. Therefore, an attempt was made to identify the exposed

planes of the Co-S15, Co-S16 and Co-S3 samples by HRTEM (Figure 10). In all cases both {311} and {220} planes could be observed, with lattice fringes of 0.245 and 0.285 nm, respectively. In addition, the presence of less abundant {111} planes, with a lattice fringe of 0.466 nm, was also evident. On the basis of the analysis of 50-70 crystallites the relative abundance of these three planes could be roughly determined. Results depicted in Figure 11 evidenced that the presence of {220} planes decreased in the following order: Co-S15(48%) > Co-S16(42%) > Co-S3(32%). This observed trend was in good agreement with the catalytic activity shown by the nanocasted Co_3O_4 catalysts. In sum, the notable catalytic performance of Co-S15 sample was related to its high oxygen adspecies concentrations and good low-temperature reducibility. These properties were in turn related to the existence of active {220} planes and a high population of Co^{2+} species at the surface, which ultimately were favoured by a relatively high surface area and a high quality 2D ordered mesoporous architecture [35-37]. On the other hand, the activity of the samples appeared to be also significantly influenced by the acid density, as revealed by the reasonably good correlation between the areal reaction rate and this property shown in Figure S6 (supplementary material). This behaviour suggested that the mechanism of the reaction is controlled by the effective chemisorption of the chlorinated feed on an acid site and the subsequent attack of easily mobile oxygen species [38,39].

FIGURE 9

FIGURE 10

FIGURE 11

Ideally, a suitable catalyst must exhibit a high activity for DCE decomposition but also be selective towards CO_2, HCl and Cl_2 when the complete destruction of the feed (>95%) is achieved. Therefore, the presence of carbon monoxide and/or small amounts

of partially oxidised hydrocarbons is not desirable. Hence, the product distribution of the hard-templated cobalt oxide catalysts was analysed. CO_2 selectivity was complete and no traces of CO were observed at any temperature. The negligible presence of CO as oxidation product is coherent with the results reported on the oxidation of hydrocarbons with varying chemical nature over Co_3O_4-based catalysts. It is noteworthy that this high selectivity to CO_2 instead of CO is found irrespective of the morphology and particle size of Co_3O_4 crystallites. Most of the investigations seem to favor a Mars-van Krevelen-type mechanism, which assumes surface oxygen ions of the Co_3O_4 catalyst participate in the CO oxidation as part of an overall reduction-oxidation cycle [40,41]. The most active sample (Co-S15) reached 100% CO_2 selectivity at 375 ºC whereas the rest of the sample needed 400-425 ºC, except for the Co-S3 sample, which required temperatures as high as 450 ºC. These activity results contrasts with those obtained with other metal oxide catalysts, such as Mn_2O_3 and CeO_2, where significant amounts of carbon monoxide are obtained [42,43]. At lower reaction temperatures (<350 ºC), although no CO was noticed, small amounts of highly chlorinated byproducts as vinyl chloride, carbon tetrachloride, tetrachloroethylene, trichloroethylene or dichloroethylene were detected. On the other hand, only HCl and Cl_2 as deep oxidation products at temperatures between 375 and 500 ºC were detected. Table 3 includes the HCl/Cl_2 molar ratio at 375 ºC. It varied between 1.3 for the Co-S15 sample and 0.8 for the Co-S16 and Co-SP oxides. The generation of large amounts of molecular chlorine was associated with the activity of Co_3O_4 in the Deacon reaction ($2HCl+½O_2 \leftrightarrow Cl_2+H_2O$). The relative abundance of HCl/Cl_2 in the exit stream increased with temperature (from 400 to 500 ºC), given that the equilibrium of the Deacon reaction was shifted towards HCl production.

Finally, attention was paid to examining the stability of the most active Co-S15 sample when operating at constant temperature during a relatively prolonged time on stream (120 h). An operation temperature of 325 ºC (with a conversion well below 100%) was selected which was suitable for observing eventual changes of the catalyst performance. Results shown in Figure 12 revealed a relatively stable conversion at about 90% and a selectivity to CO_2 close to 90%. A slight loss of activity occurred during the first reaction interval but the conversion remained roughly stable after operating for 20 h. was noted by XRD. The BET surface area decreased by about 20%, probably due to the accumulation of small amounts of carbonaceous by-products (2wt.%) as revealed by XPS, and a slight sintering. The observed enlargement of the crystallite size (14%) could be attributed to hot spots on the surface of the catalyst during reaction. As for the presence of Cl species, both EDX and XPS analysis indicated the existence of small amounts of adsorbed Cl on the sample, about 1.5wt.% and 4wt.%, respectively. Furthermore, XPS results evidenced that the abundance of Co^{2+} and O_{ads} on the surface decreased with Co^{2+}/Co^{3+} and O_{ads}/O_{latt} ratios of 1.1 and 0.9, respectively (1.2 and 1.0 for the fresh sample) (Figure S7, supplementary material). Interestingly, these minor changes did not seem to strongly influence the performance of the catalyst.

FIGURE 12

4. Conclusions

The use of hard-templating routes for the synthesis of bulk Co_3O_4 was highly promising for designing catalysts with improved physico-chemical properties for the oxidation of chlorinated compounds. Among the various mesoporous silica templates (SBA-15, SBA-16 and SBA-3), the catalyst obtained from SBA-15 was the most efficient in the oxidation of 1,2-dichloroethane.

The SBA-15 silica allowed for the preparation of a 2D ordered nanorod-like structure which was characterised by a relatively high surface area, high concentration of oxygen adspecies which was connected with an enrichment of Co^{2+} species at the surface and the existence of {220} crystal planes, and a good low-temperature reducibility. By contrast, the samples prepared from SBA-16 and SBA-3 and the catalyst obtained by silica aquagel confined precipitation exhibited a wormhole-like mesoporous structure that negatively influenced these key catalytic properties and the observed specific reaction rate. The nanocasted Co_3O_4 derived from the SBA-15 silica not only exhibited a high oxidation activity as temperatures as low as 350 ºC with a notable selectivity to CO_2 and HCl/Cl_2 as main oxidation products were obtained, but also resulted very stable during prolonged reaction time intervals.

Acknowledgements

The authors wish to thank the financial support for this work provided by the Ministry of Economy and Competitiveness (CTQ2016-80253-R), the Basque Government (Grant 2011/065, IT657-13) and the University of The Basque Country (UFI 11/39). The microscopy works have been conducted in the 'Laboratorio de Microscopías Avanzadas' at 'Instituto de Nanociencia de Aragón – Universidad de Zaragoza'. Authors acknowledge the LMA-INA for offering access to their instruments and expertise.

References

[1] E. Escalera, M.A. Ballem, J.M. Córdoba, M. Antti, M. Odén, Powder Technol. 221 (2012) 359-364.

[2] B. Solsona, T. García, R. Sanchis, M.D. Soriano, M. Moreno, E. Rodríguez-Castellón, S. Agouram, A. Dejoz, J.M. López Nieto, Chem. Eng. J. 290 (2016) 273-281.

[3] H. Gong, J. Zhu, K. Lv, P. Xiao, Y. Zhao, New. J. Chem. 39 (2015) 9380-9388.

[4] B. Solsona, T.E. Davies, T. Garcia, I. Vázquez, A. Dejoz, S.H. Taylor, Appl. Catal. B 84 (2008) 176-184.

[5] T. Garcia, S. Agouram, J.F. Sánchez-Royo, R. Murillo, A.M. Mastral, A. Aranda, I. Vázquez, A. Dejoz, B. Solsona, Appl. Catal. A 386 (2010) 16-27.

[6] J. Zhu, Q. Gao, Micropor. Mesopor. Mater. 124 (2009) 144-152.

[7] Y. Ren, Z. Ma, P.G. Bruce, Chem. Soc. Rev. 41 (2012) 4909-4927.

[8] D. Gu, F Schüth, Chem. Soc. Rev. 43 (2014) 313-344.

[9] J. González-Prior, J.I. Gutiérrez-Ortiz, R. López-Fonseca, G. Busca, E. Finocchio, B. de Rivas, Catal. Sci. Technolog. 6 (2016) 5618-5630.

[10] O. González, H. Pérez, P. Navarro, L.C. Almeida, J.G. Pacheco, M. Montes, Catal. Today. 148 (2009) 140-147.

[11] M. Mesa, L. Sierra, J.-. Guth, Micropor. Mesopor. Mater. 112 (2008) 338-350.

[12] I. López, T. Valdés-Solís, G. Marbán, ChemCatChem. 3 (2011) 734-740.

[13] J. González-Prior, R. López-Fonseca, J.I. Gutiérrez-Ortiz, B. de Rivas, Appl. Catal. B 199 (2016) 384-393.

[14] A. Feliczak-Guzik, B. Jadach, H. Piotrowska, M. Murias, J. Lulek, I. Nowak, Micropor. Mesopor. Mater. 220 (2016) 231-238.

[15] P.I. Ravikovitch, A.V. Neimark, J. Phys. Chem. B 105 (2001) 6817-6823.

[16] M.V. Ponte, L.P. Rivoira, J. Cussa, M.L. Martínez, A.R. Beltramone, O.A. Anunziata, Micropor. Mesopor. Mater. 227 (2016) 9-15.

[17] E. Rombi, M.G. Cutrufello, L. Atzori, R. Monaci, A. Ardu, D. Gazzoli, P. Deiana, I. Ferino, Appl Catal A Gen. 515 (2016) 144-153.

[18] Djinovic, P., Batista, J, Levec, J., Pintar, A., Appl. Catal. A 364 (2009) 156-165.

[19] S. Zuo, F. Liu, J. Tong, C. Qi, Appl Catal A 467 (2013) 1-6.

[20] Y. Du, Q. Meng, J. Wang, J. Yan, H. Fan, Y. Liu, H. Dai, Micropor. Mesopor. Mater. 162 (2012) 199-206.

[21] S.A. Singh, G. Madras, Appl. Catal. A 504 (2015) 463-475.

[22] C. Liu, Q. Liu, L. Bai, A. Dong, G. Liu, S. Wen, J. Mol. Catal. A 370 (2013) 1-6.

[23] X. Zhang, P. Zhang, H. Yu, Z. Ma, S. Zhou, Catal Lett. 145 (2015) 784-793.

[24] M. Králik, Z. Vallušová, P. Major, A. Takácová, M. Hronec, D. Gašparovicová, Chem. Pap. 68 (2014) 1690-1700.

[25] G. Bai, H. Dai, J. Deng, Y. Liu, F. Wang, Z. Zhao, W. Qiu, C.T. Au, Appl. Catal. A 450 (2013) 42-49.

[26] S. Esposito, A. Setaro, P. Maddalena, A. Aronne, P. Pernice, M. Laracca, J. Sol-Gel Sci. Technol. 60 (2011) 388-394.

[27] K .Shojaee, B.S. Haynes, A. Montoya, Proceeding of the Combustion Institute 36 (2017) 4365-4373.

[28] Y. Zhang, A. Wang, Y. Huang, Q. Xu, J. Yin, T. Zhang, Catal. Lett. 142 (2012) 275-281.

[29] C. Ma, Z. Mu, C. He, P. Li, J. Pi, Z. Hao, J. Environ. Sci. 23 (2011) 2078-2086.

[30] B. Bai, H. Arandiyan, J. Li, Appl Catal B 142-143 (2013) 677-683.

[31] P. Yang, S. Zuo, Z. Shi, F. Tao, R. Zhou, Appl. Catal. B 191 (2016) 53-61.

[32] P. Yang, S. Zuo, R. Zhou, Chem. Eng. J. 323 (2017) 160-170.

555 [33] J. Yongchang, W. Shuyuan, L. Jiqing, L. Mengfei, Chem. Res. Chin. Univ. 32
556 (2016) 808-811.
557 [34] W.J. Xue, Y.F. Wang, P. Li, Z-T. Liu, Z.P. Hao, C.Y. Ma, Catal. Commun. 12
558 (2011) 1256-1268.
559 [35] L.F. Liotta, M. Ousmane, G. Di Carlo, G. Pantaleo, G. Deganello, G. Marcì, L.
560 Retailleau, A. Giroir-Fendler, Appl. Catal. A 347 (2008) 81-88.
561 [36] J. Taghavimoghaddam, G.P. Knowles, A.L. Chaffee, J. Mol. Catal. A 358 (2012)
562 79-88.
563 [37] H. Song, U.S. Ozkan, J. Catal. 261 (2009) 66-74.
564 [38] R. López-Fonseca, B. de Rivas, J.I. Gutiérrez-Ortiz, A. Aranzabal, J.R. González-
565 Velasco, Appl. Catal. B 41 (2003) 31-42.
566 [39] B. de Rivas, C. Sampedro, M. García-Real, R. López-Fonseca y J.I. Gutiérrez-
567 Ortiz, Appl. Catal. B 129 (2013) 225-235.
568 [40] P. Broqvist, I. Panas, H. Persson, J. Catal. 201 (2002) 198-206.
569 [41] S. Sun, Q. Gao, H. Wang, J. Zhu, H. Guo, Appl. Catal. B 97 (2010) 284-291.
570 [42] B. de Rivas, C. Sampedro, E.V. Ramos-Fernández, R. López-Fonseca, J. Gascon,
571 M. Makkee, J.I. Gutiérrez-Ortiz, Appl. Catal. A 456 (2013) 96-104.
572 [43] J.I. Gutiérrez-Ortiz, R. López-Fonseca, U. Aurrekoetxea, J.R. González-Velasco,
573 J. Catal. 218 (2003) 148-154.
574

CAPTIONS FOR TABLES AND FIGURES

Table 1. Textural and structural properties of the hard-templated Co_3O_4 samples.

Table 2. XPS surface composition and reducibility of the hard-templated Co_3O_4 samples.

Table 3. Catalytic results of the oxidation of DCE over of the hard-templated Co_3O_4 samples.

Figure 1. TEM images of silica templates: a) SBA-3, b) SBA-15, c) SBA-16.

Figure 2. XRD patterns of the hard-templated Co_3O_4 samples.

Figure 3. TEM images of the hard-templated Co_3O_4 samples: a) Co-S15, b) Co-S3, c) Co-S16, d) Co-SP, e) Co-S15(0.4).

Figure 4. O 1s and Co $2p^{3/2}$ XPS spectra of the hard-templated Co_3O_4 samples.

Figure 5. Redox behaviour of the hard-templated Co_3O_4 samples.

Figure 6. FT-IR skeletal spectra of the hard-templated Co_3O_4 samples.

Figure 7. Temperature-programmed reaction of adsorbed ammonia followed by thermogravimetry coupled to mass spectrometry.

Figure 8. Conversion of DCE to CO_2 over the hard-templated Co_3O_4 samples.

Figure 9. Relationship of the areal reaction rate at 250 ºC with the O_{ads}/O_{latt} ratio and the Co^{2+}/Co^{3+} ratio for the hard-templated Co_3O_4 samples.

Figure 10. HRTEM images of the hard-templated Co_3O_4 samples: a) and b) Co-S15, c) Co-S3, d) Co-S16.

Figure 11. Relative abundance of exposed planes (HRTEM) of the Co-S15, Co-S16 and Co-S3 samples.

Figure 12. Stability in DCE oxidation at 325 ºC over the Co-S15 sample for 120 h.

600

Catalyst	BET surface area, $m^2 g^{-1}$	Pore volume, $cm^3 g^{-1}$	Maxima in the pore size distribution, Å	Crystallite size, nm	Amount of residual SiO_2, %	Total acidity, mmol NH_3 g^{-1}	Acid density, mmol NH_3 m^{-2}
SBA-3	257	0.68	125	-	-	-	
SBA-15	749	0.71	39	-	-	-	
SBA-16	785	0.61	39	-	-	-	
Co-S15	83	0.18	35	16	2.3	0.46	$5.5 \cdot 10^{-3}$
Co-S3	53	0.25	160/232	26	1.2	0.31	$5.8 \cdot 10^{-3}$
Co-S16	123	0.26	53/62	12	3.6	0.54	$4.4 \cdot 10^{-3}$
Co-SP	111	0.18	35/62	13	6.9	0.29	$2.6 \cdot 10^{-3}$
Co-S15(0.4)	62	0.13	35	29	1.6	0.30	$4.8 \cdot 10^{-3}$

601 Table 1

Catalyst	Surface O_{ads}/O_{latt}	Surface Co^{2+}/Co^{3+}	H_2 consumption		
			1st peak, ºC	2º peak, ºC	%reduction
Co-S15	0.98	1.20	250	355, 300 sh	100
Co-S3	0.76	0.98	275	360, 320 sh	100
Co-S16	0.83	1.04	265	395, 300 sh	99
Co-SP	0.64	0.80	285	475	90
Co-S15(0.4)	0.91	1.16	250-280	310-355	100

sh: shoulder

Table 2

607

608

Catalyst	Areal reaction rate, mmol m^{-2} h^{-1}	T_{50}, ºC	T_{90}, ºC	S_{CO2}, % (375 ºC)	HCl/Cl_2 (375 ºC)
Co-S15	0.260	285	320	100	1.3
Co-S3	0.213	315	375	95	1.0
Co-S16	0.224	305	355	97	0.8
Co-SP	0.125	320	390	92	0.8
Co-S15(0.4)	0.246	300	340	99	1.1

609

610 Table 3

611

612

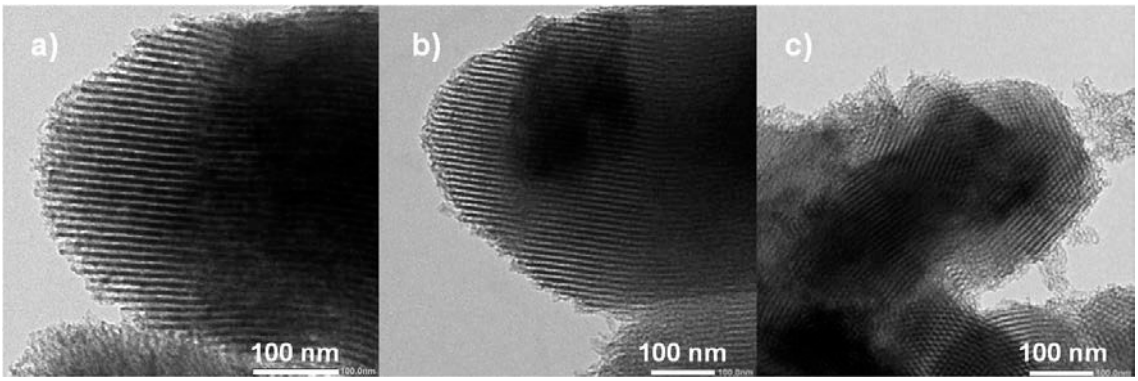

613

614 Figure 1

615

616

617

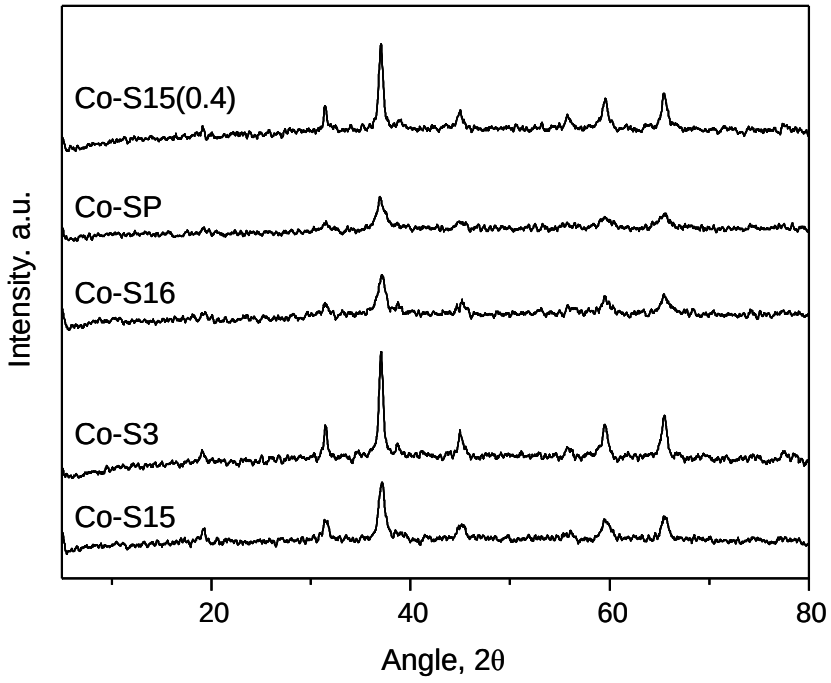

618

619 Figure 2

620

621

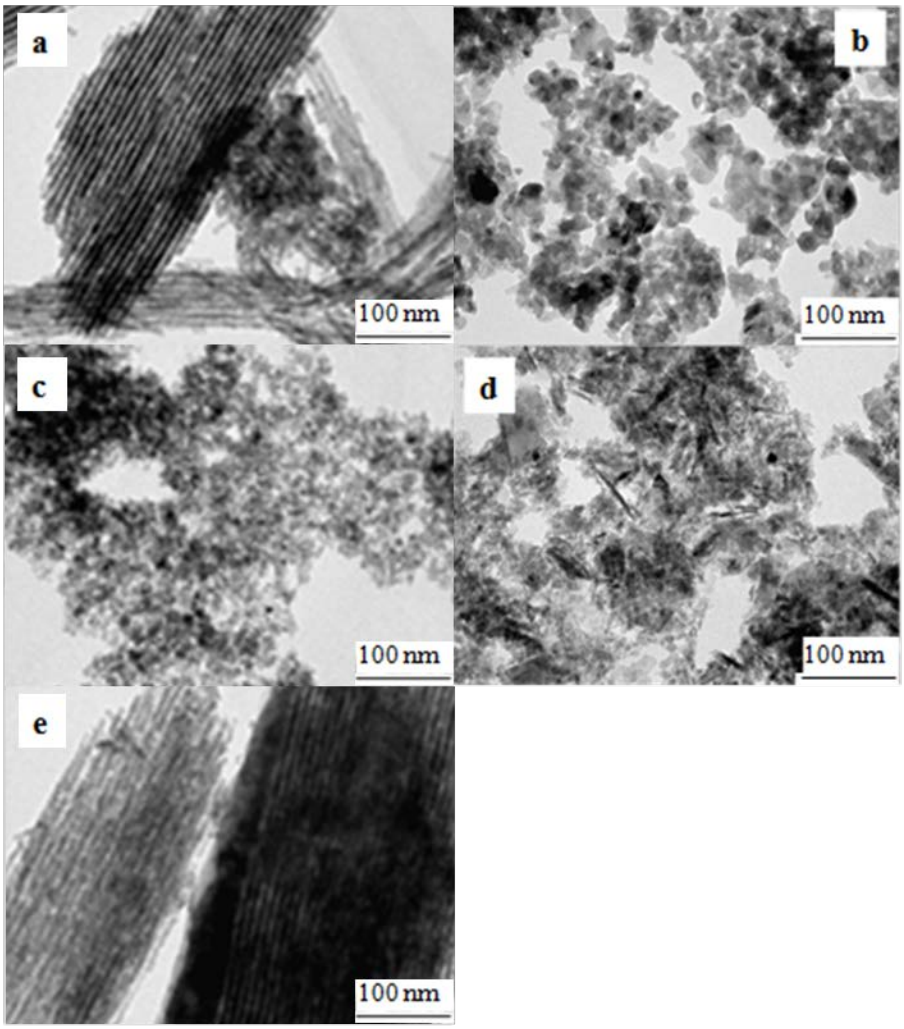

622

623 Figure 3

624

625

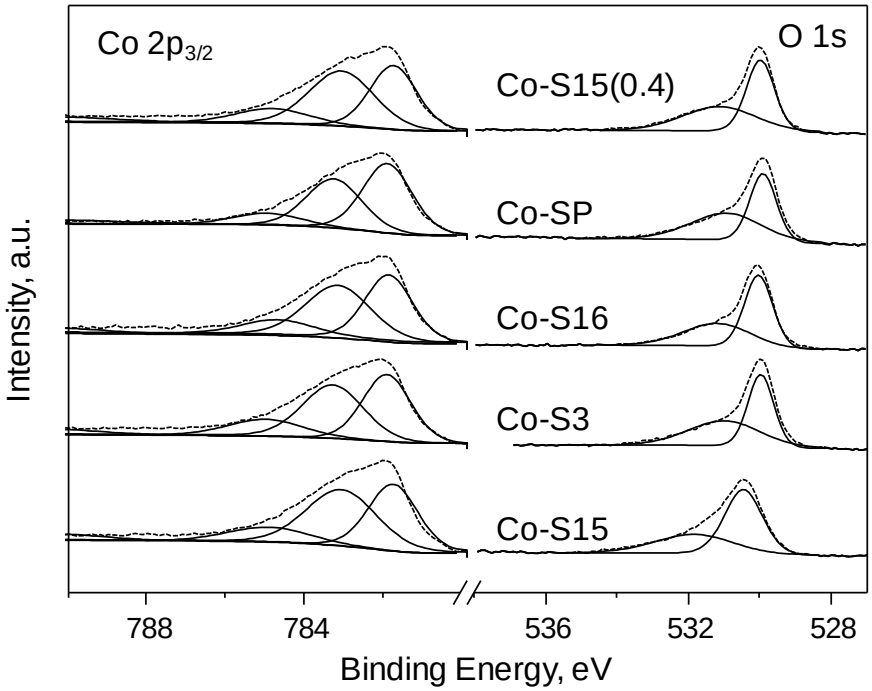

626

627 Figure 4

628

629

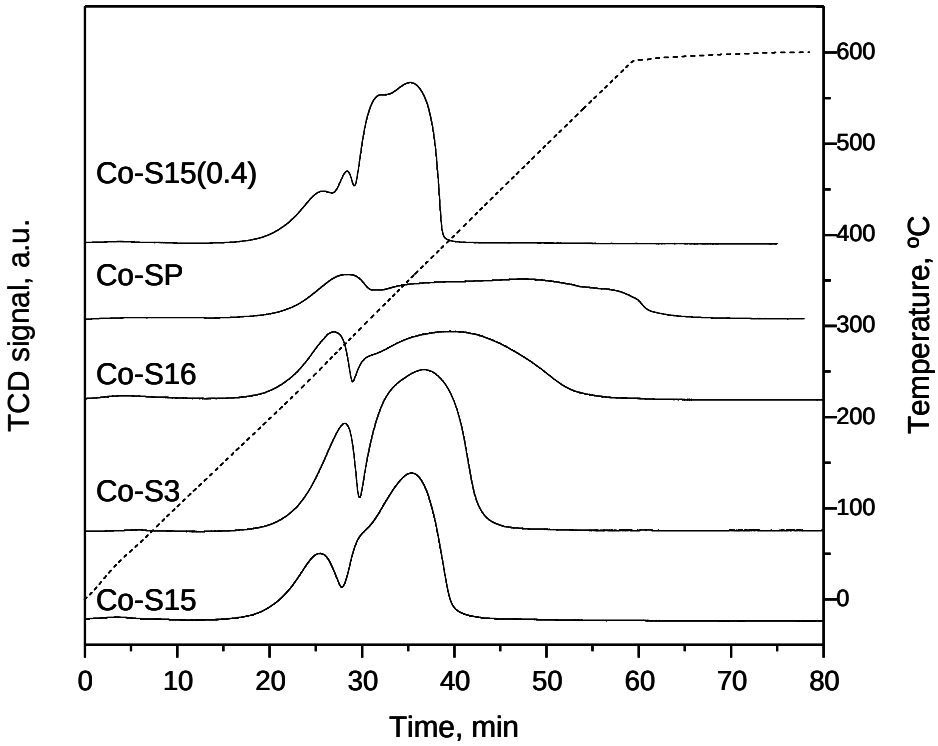

630

631 Figure 5

632

633

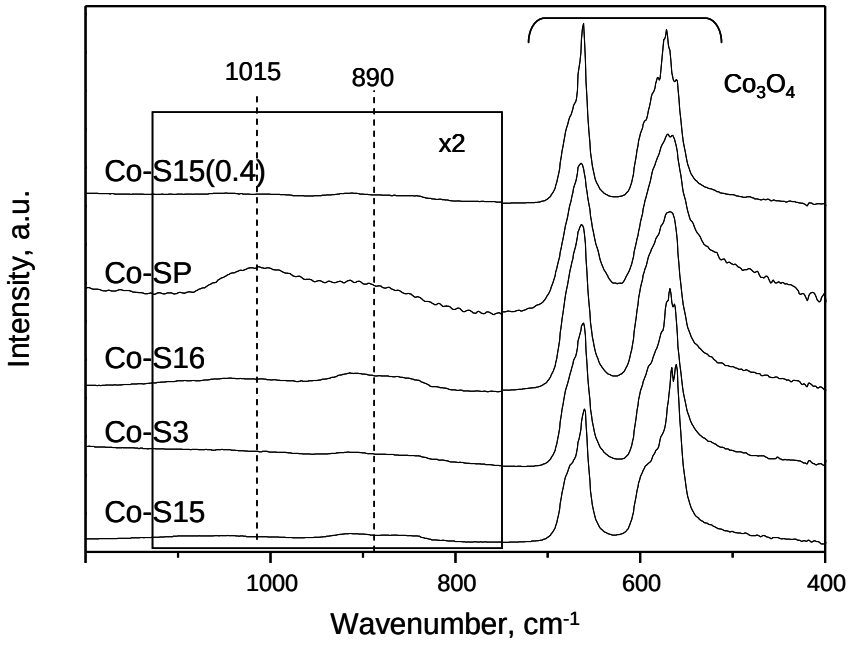

634

635 Figure 6

636

637

638

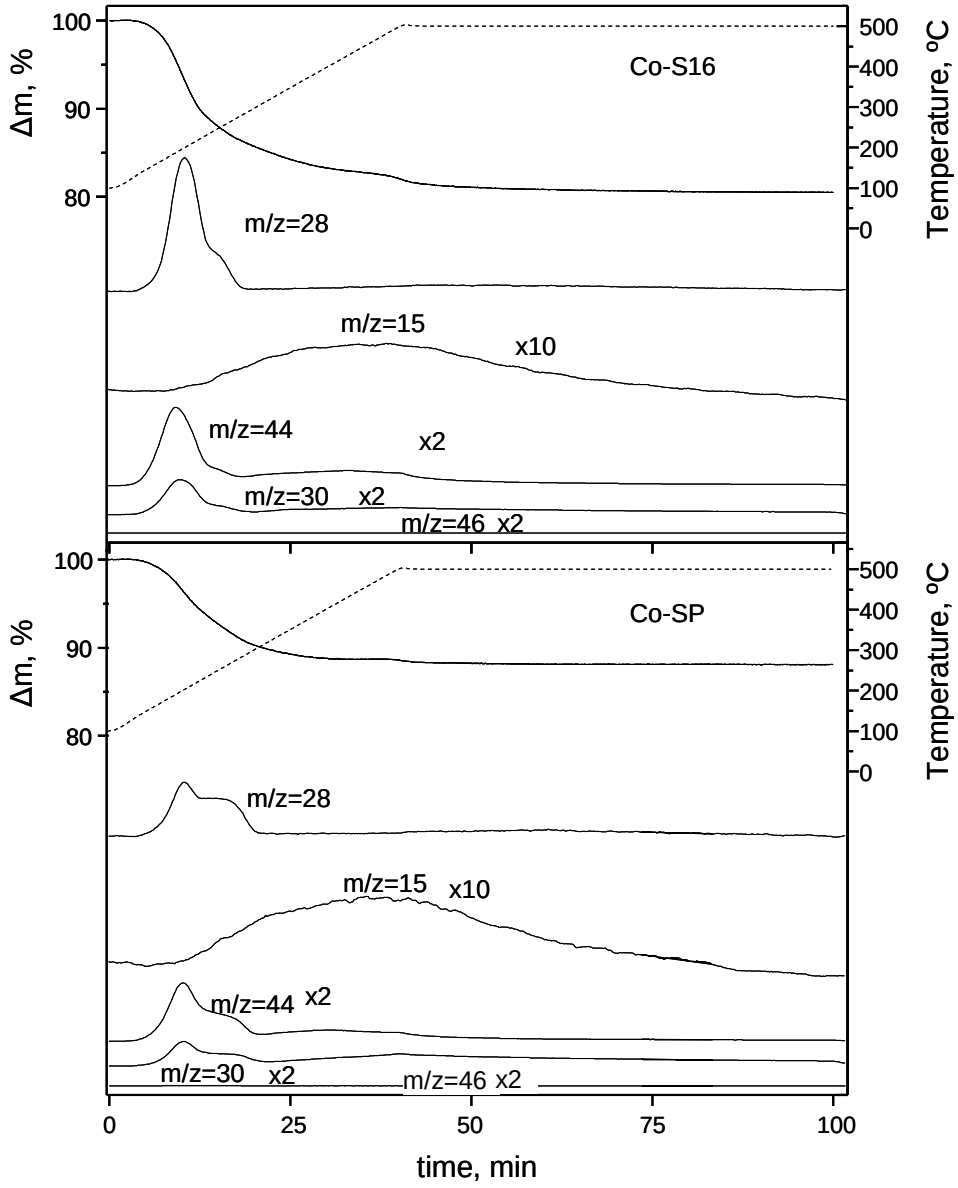

639

640 Figure 7

641

642

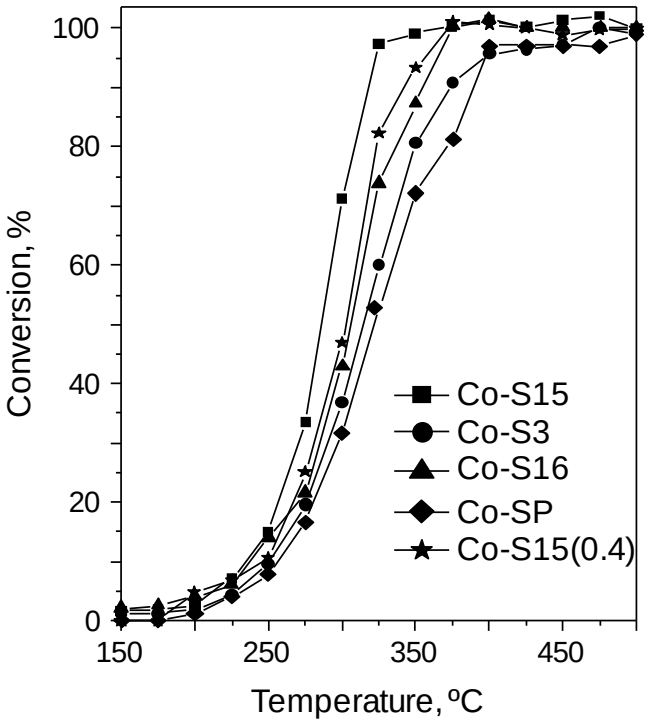

643

644 Figure 8

645

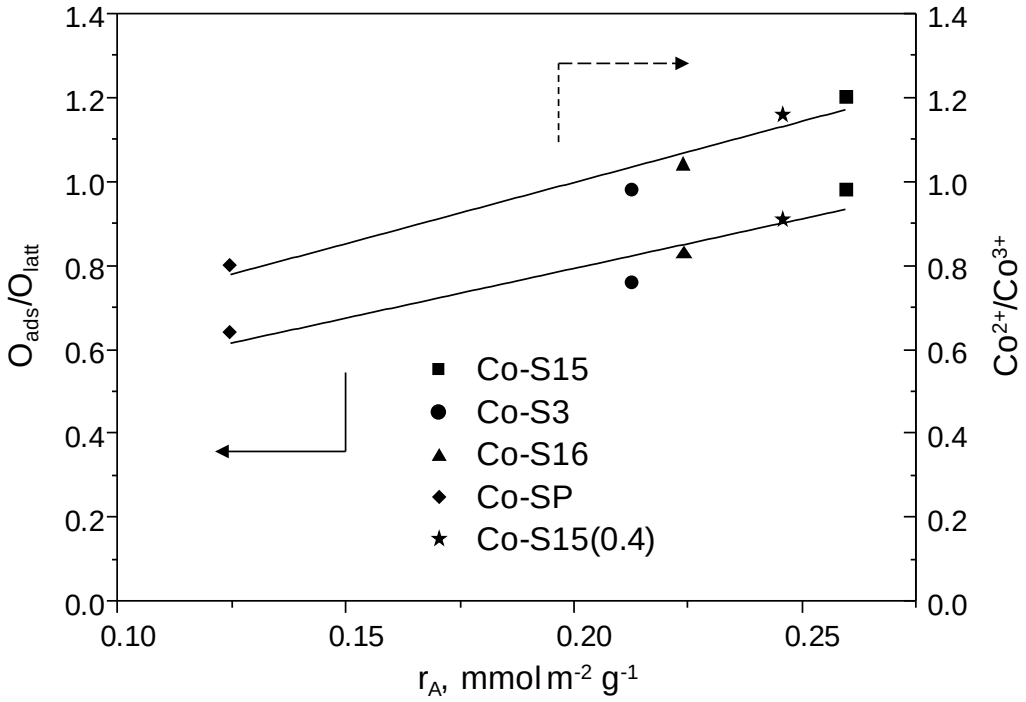

646

647 Figure 9

648

649

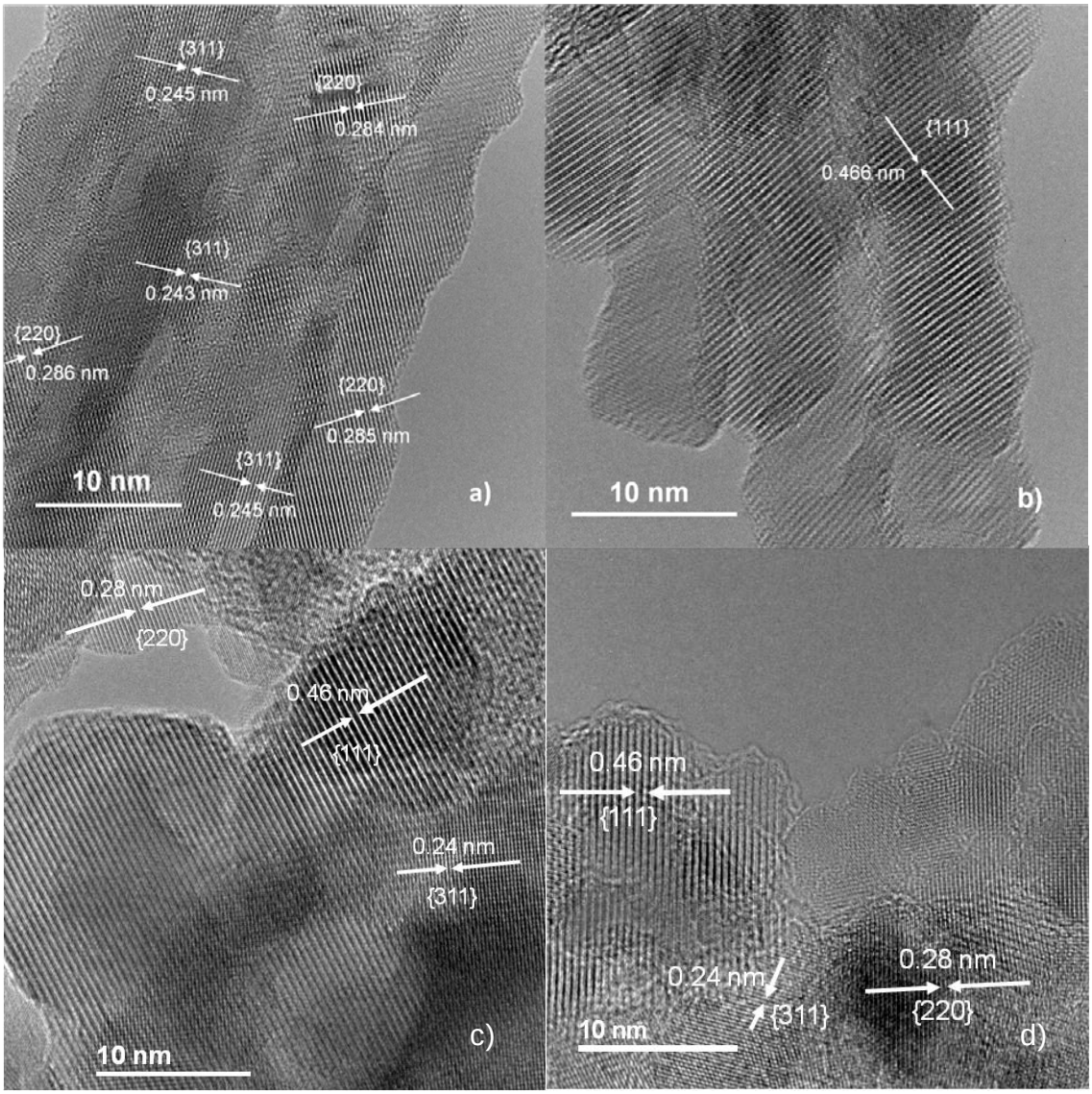
{311}
0.245 nm
{220}
0.284 nm
{311}
0.243 nm
{220}
0.286 nm
{220}
0.285 nm
{311}
0.245 nm
10 nm
a)
{111}
0.466 nm
10 nm
b)
0.28 nm
{220}
0.46 nm
{111}
0.24 nm
{311}
10 nm
c)
0.46 nm
{111}
0.24 nm
{311}
0.28 nm
{220}
10 nm
d)

Figure 10

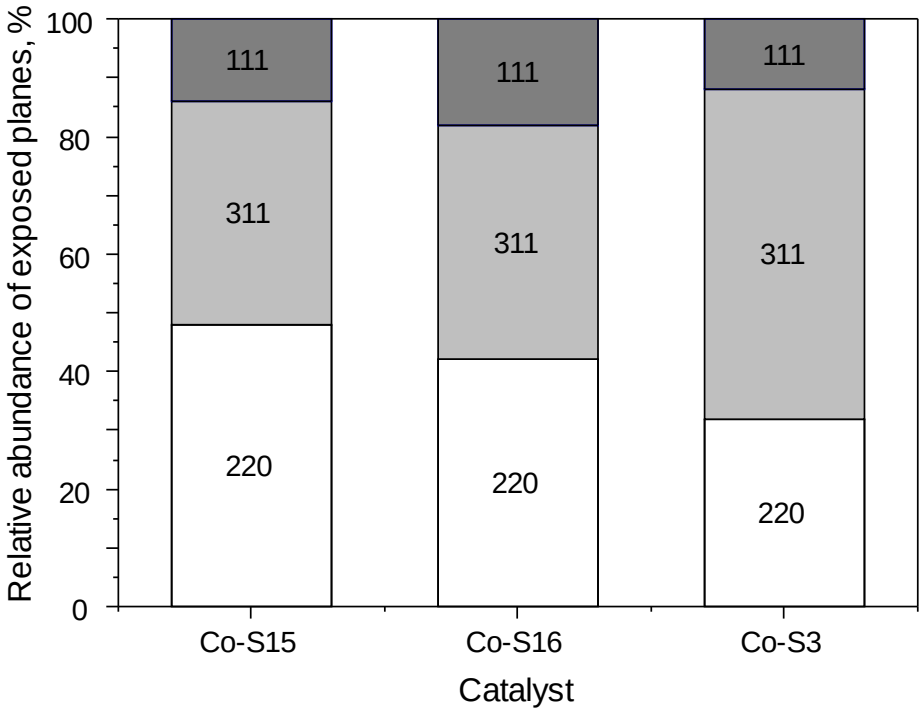
Relative abundance of exposed planes, %
100
80
60
40
20
0
111
311
220
111
311
220
111
311
220
Co-S15
Co-S16
Co-S3
Catalyst

Figure 11

657

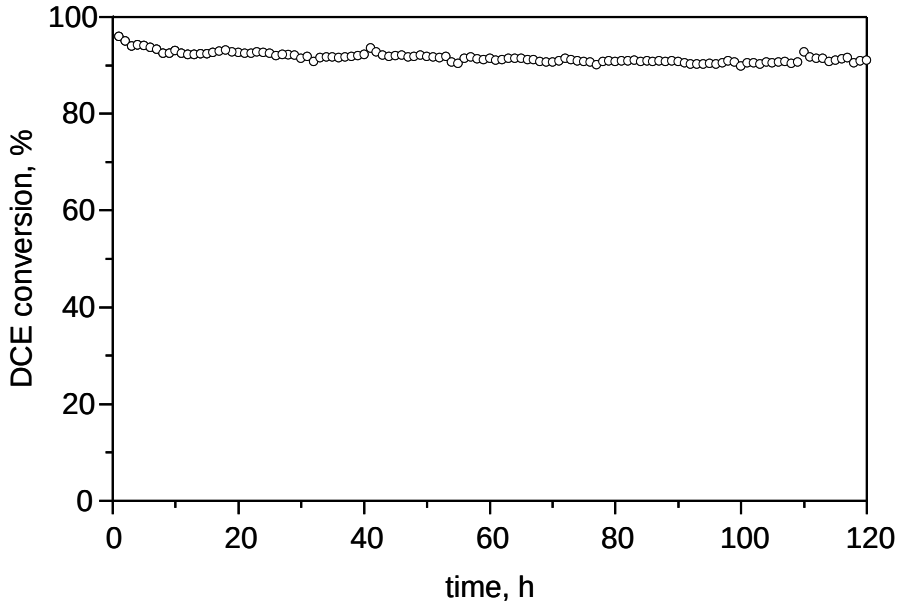

658

659 Figure 12